Surface Chemistry of a Halogenated Borazine: From Supramolecular Assemblies to a Random Covalent BN-Substituted Carbon Network

Birce Sena Tömekce,[a] Marc G. Cuxart,[a] Laura Caputo,[b] Daniele Poletto,[c] Jean-Christophe Charlier,*[b] Davide Bonifazi,*[c] and Willi Auwärter*[a]

The on-surface synthesis strategy has emerged as a promising route for fabricating well-defined two-dimensional (2D) BN-substituted carbon nanomaterials with tunable electronic properties. This approach relies on specially designed precursors and requires a thorough understanding of the on-surface reaction pathways. It promises precise structural control at the atomic scale, thus complementing chemical vapor deposition (CVD). In this study, we investigated a novel heteroatomic precursor, tetrabromoborazine, which incorporates a BN core and an OH group, on Ag(111) using low temperature scanning tunnelling microscopy/spectroscopy (LT-STM/STS) and X-ray photoelectron spectroscopy (XPS). Through sequential temperature-induced reactions involving dehalogenation and dehydro-genation, distinct tetrabromoborazine derivatives were produced as reaction intermediates, leading to the formation of specific self-assemblies. Notably, the resulting intricate supramolecular structures include a chiral kagomé lattice composed of molecular dimers exhibiting a unique electronic signature. The final product obtained was a random covalent carbon network with BN-substitution and embedded oxygen heteroatoms. Our study offers valuable insights into the significance of the structure and functionalization of BN precursors in temperature-induced on-surface reactions, which can help future rational precursor design. Additionally, it introduces complex surface architectures that offer a high areal density of borazine cores.

Introduction

Hybrid boron nitrogen carbon (BNC) materials are promising for future use in semiconducting electronic devices and optoelectronics applications, particularly by offering band gap tunability.[1–4] The isostructural and isoelectronic nature of C—C and B—N bonds should facilitate the synthesis of BNC layers within a sp^2-bonded honeycomb atomic structure, a common feature of graphene and hexagonal boron nitride (hBN). Considerable efforts have been made to realize such hybrid 2D materials, employing different strategies, including CVD.[5–9]

[a] B. Sena Tömekce, M. G. Cuxart, W. Auwärter
Physics Department E20, TUM School of Natural Sciences, Technical University of Munich, Garching, Germany
E-mail: wau@tum.de

[b] L. Caputo, J.-C. Charlier
Institute of Condensed Matter and Nanosciences, Université catholique de Louvain (UCLouvain), 1348 Louvain-la-Neuve Belgium
E-mail: jean-christophe.charlier@uclouvain.be

[c] D. Poletto, D. Bonifazi
Institute of Organic Chemistry, Faculty of Chemistry, University of Vienna, Vienna, Austria
E-mail: davide.bonifazi@univie.ac.at

However, the resulting nanomaterials, in general, are lacking long-range order and structural quality, e.g., forming disordered BNC alloys,[6,7] or suffering from the segregation of BN domains within graphene patches.[5,8,9] The high temperatures usually employed in these procedures contribute to the limited structural control and reproducibility. Nonetheless, for some systems, nanoscale patterning was achieved by a CVD approach. A pioneering study introduced hexamethyl borazine to synthesize BN-doped graphene, termed h-BNC, on Ir(111).[3] The same substrate was recently used to introduce arrays of individual B atoms in a corrugated graphene sheet.[10] Achieving a regular doping pattern with atomic precision in 2D hybrid materials is key to engineer, control, and fully exploit the properties of such systems. A promising strategy to tackle this still unsolved challenge bases on polycyclic aromatic hydrocarbons, or nano-graphenes, doped with borazine (B_3N_3) units.[11–14] Through surface-assisted reactions proceeding at moderate temperatures in a controlled ultrahigh vacuum (UHV) environment, these tailor-made molecular precursors are anticipated to lead to atomically-defined 2D BN-substituted nanostructures, mirroring the successful on-surface fabrication of all-carbon materials, such as graphene nanoribbons,[15] nanoporous graphene,[16,17] and other graphene nanostructures.[18] Indeed, a BN-containing covalent 2D porous network[19] and 1D nanoribbons[2,20] were achieved on noble metal supports. These systems complement B- or N-substituted carbon nanostructures[21–23] and supramolecular, self-assembled borazine-based architectures.[24–28] Nonetheless, extended, 2D covalent networks including well-separated borazine units remain elusive so far.

Chemistry–A European Journal

Research Article
doi.org/10.1002/chem.202402492

**Chemistry
Europe**
European Chemical
Societies Publishing

Here, we introduce a novel borazine precursor with distinct functionalities to explore temperature-induced, sequential intramolecular and intermolecular ring-closing reactions, to characterize the concomitant molecular conformations, and to rationalize the resulting supramolecular assemblies and covalent networks. Specifically, B,B′-Bis(2,6-dibromophenyl)-B″-hydroxy-N,N′,N″-triphenylborazine, further referred to as "tetrabromoborazine" is applied on Ag(111), with a comprehensive interface characterization based on LT-STM/STS and XPS. The precursor features a borazine core and terminal Br- and OH-functionalization, thus enabling dehalogenation as well as dehydrogenation reactions. With this precursor design, we aim to introduce additional functional groups into covalent networks and to probe the effect of defects, such as oxygen heteroatoms, that can enrich the properties of the resulting nanostructures. The synthesis of the precursor is described in the Supporting Information. Complementary insight into the structure of the precursor and selected reaction products is provided by density functional theory (DFT).

Results and Discussion

Temperature-Induced On-Surface Reactions and Self-Assemblies

To explore the on-surface reactions of tetrabromoborazine on Ag(111) and to characterize the respective molecular structures and assemblies, the molecule was studied over a wide temperature range. Scheme 1 sketches the molecular structures, from the lowest explored temperature ($-60\,°C$) to the highest applied temperature ($410\,°C$), and highlights the respective on-surface reactions, namely debromination, cyclodehydrogenation (ring-closing), and intermolecular covalent coupling, respectively.

Figure 1 shows STM images after deposition of a sub-monolayer of tetrabromoborazine on the Ag(111) substrate kept at $-60\,°C$. Extended, highly regular self-assembled islands are formed, which can be described by a rhomboid unit cell containing four molecules (parameters: $a = 2.42 \pm 0.05$ nm, $b = 2.01 \pm 0.05$ nm, $\theta = 80 \pm 3°$, area $= 4.8 \pm 0.2$ nm^2, molecular pack-

ing density 0.84 molecule/nm^2, see Figure 1b). Three domain orientations, following the three dense-packed crystallographic directions of the Ag(111) lattice are observed. STM imaging with sub-molecular resolution allows to identify individual molecular units in the assembly and reveals two prominent protrusions, each adjacent to a faint protrusion, for each molecule (see blue dashed outlines in Figure 1b). Based on the molecular dimensions, the two prominent protrusions are attributed to the terminal Br atoms decorating phenyl groups 2 and 4 (see inset in Figure 1a). The Br atoms dominate the STM contrast due to their larger atomic size compared to the rest of elements present in the molecule[29] and the tilt of the phenyl rings. The STM images evidence subtle contrast differences of these protrusions within the molecular layer, suggesting slight variations in the tilt angles of the brominated phenyl groups (structural model, inset, Figure 1a). Indeed, DFT-optimized structures of intact tetrabromoborazine in gas phase reveal minor energy differences between configurations with different phenyl tilt angles (see Supporting Information, Figure S1). As will be discussed below, XPS Br 3d core level spectra confirm that tetrabromoborazine adsorbs intact on Ag(111) at low temperature ($-50\,°C$), corroborating the above interpretation of the STM data. STS measurements, giving access to the interfacial electronic structure, indicate that the intact tetrabromoborazine interacts rather weakly with the Ag(111) support. A spectral series is presented in Figure S2, showing an interface state on the molecular islands that is upshifted by about 130 meV with respect to the surface state onset on bare Ag(111).

Aiming for debromination and cyclodehydrogenation reactions, tetrabromoborazine was annealed to moderate temperatures ($170\,°C$–$220\,°C$), after room temperature deposition on Ag(111). Indeed, STM images show supramolecular assemblies distinctly different from the one achieved by low-temperature deposition. Figure 2, representing an annealing temperature of $170\,°C$, shows the coexistence of two distinct assemblies, a chiral kagomé phase and a hexagonal array, with the latter phase constituting the majority (Figure 2a). High-resolution images reveal that the kagomé phase is constituted by dimers and individual monomers. The centres of the dimers represent the vertices of a porous kagomé lattice, with the hexagonal
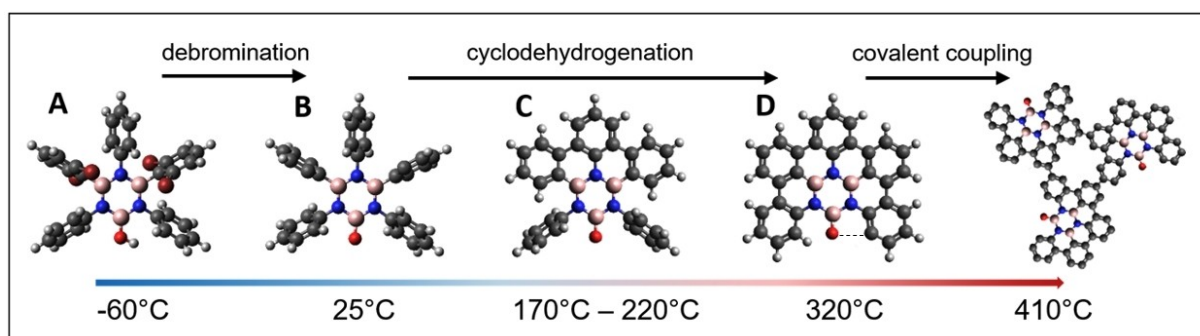
Scheme 1. Atomistic models of (A) unreacted tetrabromoborazine and (B–D) selected reaction products. The figure covers the experimentally accessed temperature range (bottom) and the corresponding on-surface reaction steps (top), activated upon thermal annealing. Dark grey, dark red, pink, blue, red and white correspond to C, Br, B, N, O, and H, respectively.
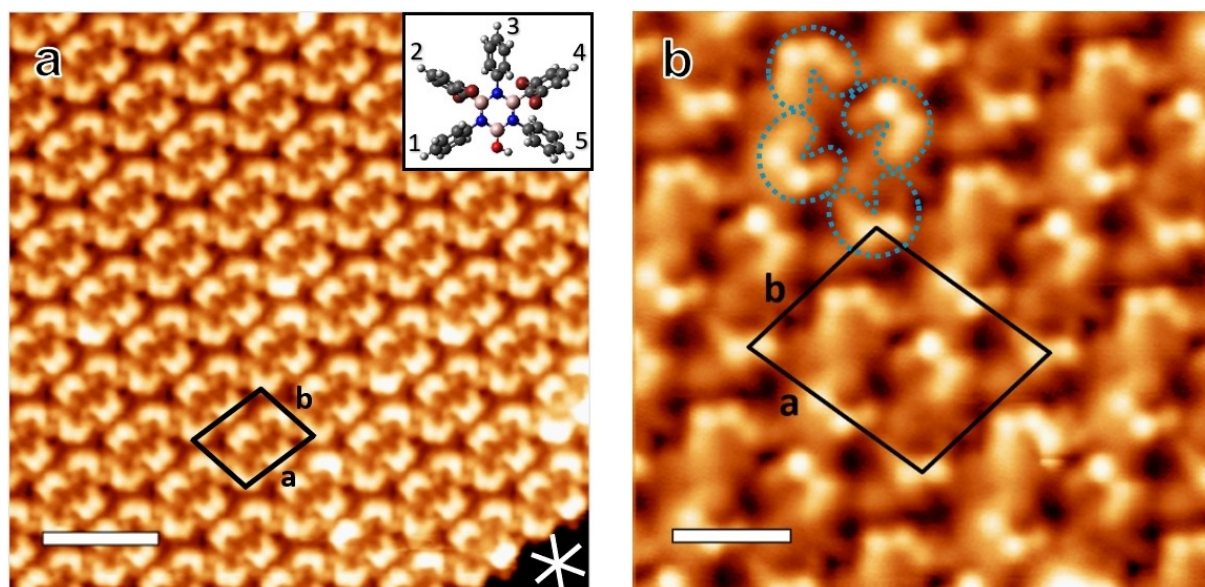
Chem. Eur. J. **2024**, *30*, e202402492 (2 of 9)

© 2024 The Author(s). Chemistry - A European Journal published by Wiley-VCH GmbH

Chemistry–A European Journal

Research Article
doi.org/10.1002/chem.202402492

Chemistry
Europe
European Chemical
Societies Publishing

Figure 1. STM images of self-assembled arrays of intact tetrabromoborazine on Ag(111), prepared by deposition at −60 °C. (a) Large scale image including the unit cell (black rhomboid). The white lines indicate the three dense-packed crystal directions of the Ag(111) lattice. The inset shows a structural model with slight variations in the (out of plane) tilt angles of the rings, which are numbered from 1 to 5 for identification. (Image parameters: I_t: 44 pA, V_b: 71 mV, scale bar: 3.6 nm). (b) STM image with submolecular resolution. The blue dashed outlines highlight individual tetrabromoborazine molecules, with the bright protrusions attributed to the Br atoms attached to the tilted phenyl rings. The unit cell contains four molecules. (Image parameters: I_t: 150 pA, V_b: 28 mV, scale bar: 1.3 nm).
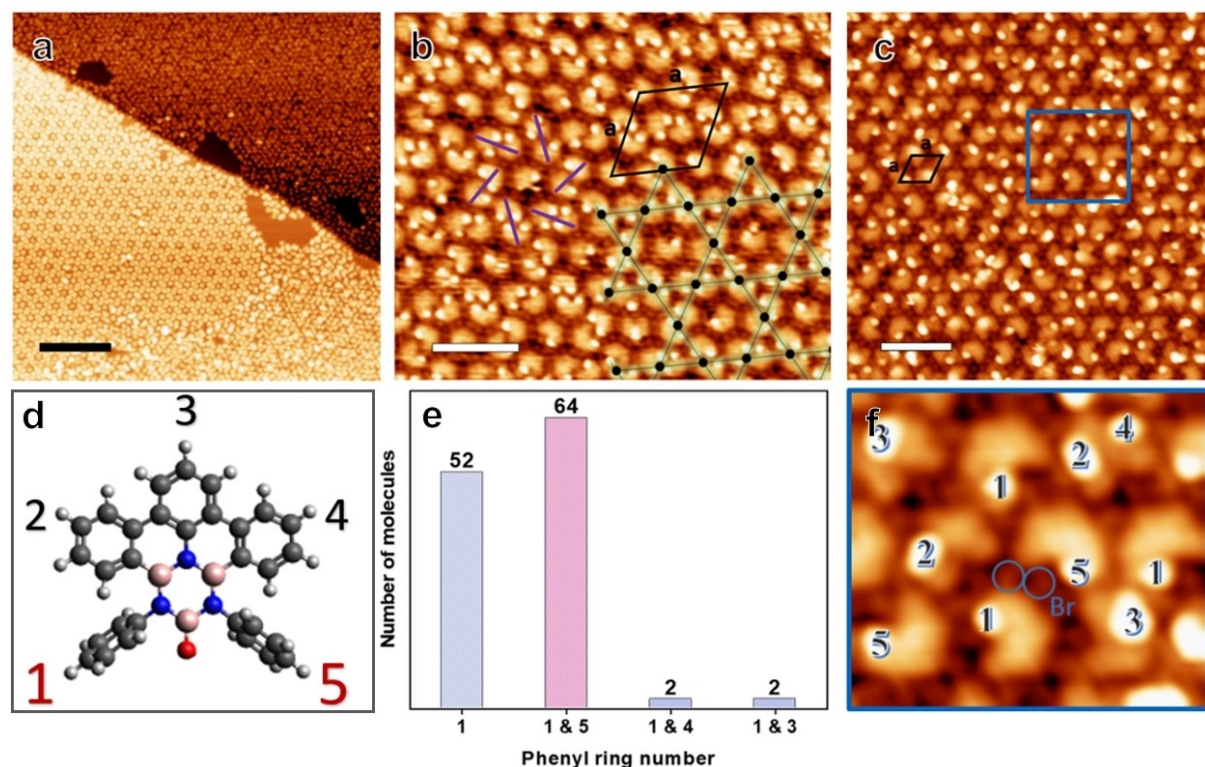

Figure 2. (a) STM image of the coexisting self-assemblies, i.e., the kagomé and hexagonal phase, observed after annealing at 170 °C. (b) STM image of the kagomé phase. The overlayed kagomé lattice points (black dots) are located at the centers of the dimers. The counter clockwise chirality of this domain is indicated by purple lines, the unit cell is represented by the black rhombus. (c) STM image of the hexagonal phase. (d) Molecular model with the numbering of the phenyl rings. (e) Histogram showing the statistics of the tilted phenyl rings of the dimers counted from the kagomé phase in (b). (f) Zoom-in STM image of the area marked by a blue rectangle, highlighting the tilted phenyl rings (numbered accordingly) and showing the cleaved off Br atoms. (Image parameters (a) I_t: 0.16 nA, V_b: 1 V, scale bar: 20 nm, (b) I_t: 0.11 nA, V_b: 1.08 V, scale bar: 4.5 nm, (c) I_t: 0.13 nA, V_b: 0.82 V, scale bar: 4.1 nm.)

Chem. Eur. J. **2024**, *30*, e202402492 (3 of 9)

© 2024 The Author(s). Chemistry - A European Journal published by Wiley-VCH GmbH

Chemistry–A European Journal

Research Article
doi.org/10.1002/chem.202402492

Chemistry
Europe
European Chemical
Societies Publishing

voids occupied by monomers (Figure 2b). The area of the unit cell is 16.0 ± 0.7 nm² with lattice parameters of $a = 4.3 \pm 0.09$ nm and $\theta = 60 \pm 3°$, corresponding to the molecular packing density of 0.44 molecules/nm². On first sight, the hexagonal arrays (Figure 2a and c) seem poorly ordered. However, FFT images of the STM data confirm the hexagonal symmetry (see Figure S3). The rhombic unit cell has an area of 2.2 nm² with $a = 1.6 \pm 0.05$ nm, yielding a packing density of 0.45 molecules/nm².

Additional insight is gained from STM images providing submolecular resolution. For both, the kagomé and the hexagonal phase, protrusions are observed at specific positions of the molecule, with the number of protrusions per molecule ranging from zero to two. Independent of the number of protrusions, the molecules feature a U-shape, distinct from the one observed for the non-debrominated case. As it will be shown below by XPS, debromination is completed at these temperatures. Accordingly, in contrast to the case of pristine tetrabromoborazine, these new protrusions are not attributed to Br, but rather to tilted phenyl rings alone. Thus, a molecule lacking any protrusions is assigned to a fully planarized tetrabromoborazine derivative, i.e., a molecule that underwent debromination and complete cyclodehydrogenation. One protrusion per molecule signals one tilted phenyl ring, two protrusions per molecule signal two tilted phenyl rings. The STM data in Figure 2 thus reveal that cyclodehydrogenation is neither completed at 170 °C nor at 220 °C, despite full debromination. Furthermore, the positions and numbers of protrusions define distinct molecular conformations. The protrusions are numbered from 1 to 5, reflecting the positions of the tilted phenyl rings (see Figure 1a and Figure 2d). Interestingly, the kagomé phase and the hexagonal phase differ in their composition. A statistical analysis shows a broad variety of conformations in the hexagonal phase, e.g., including a large percentage of monomers with a single tilted ring on position 3, or a pair of tilted rings on positions 2 and 4 (see Figure S3). In stark contrast, the conformation of the dimers constituting the kagomé lattice is more homogenous. First, the vast majority of dimers is formed by molecules featuring protrusions on position

1 and/or position 5, i.e., by molecules with tilted "terminal" rings. Among them, 60% have four tilted phenyl rings (number 1 and 5 in both molecules), 20% contain three tilted phenyl rings, and the remaining 20% are formed by molecules both having only one terminal ring tilted. Second, the chirality of the kagomé lattice, given by the relative lateral positions of the molecules constituting the dimers, is related to the molecular conformation. For domains with a "clockwise" dimer configuration (see Figure 2b, purple lines), single protrusions are only observed on ring 1. For domains with a "counter-clockwise" dimer configuration, single protrusions are only observed on ring 5 (see Figure S4). Accordingly, the molecular assemblies are linked to the conformation of the constituting molecules and the coexistence of the two phases can be rationalized by the occurence of distinct, partially planarized monomers on the surface. For both phases, individual protrusions assigned to Br atoms are observed in between the molecules (Figure 2b, c, f), consistent with previous reports on debrominated precursors on Ag(111).[30] Note that hydrogen passivation of the unreacted radical sites is expected for the reactions intermediates (e.g., species C in Scheme 1 and Figure 2).[31] A more detailed discussion of the intriguing kagomé phase, including dimer structure and electronic properties, is provided below in a separate section.

To promote complete cyclodehydrogenation and concomitant full planarization, higher annealing temperatures were applied. Complete planarization of all molecules is achieved at 320 °C. Figure 3a shows an STM image of a resulting quasi-hexagonal array of planarized molecules. Clearly, pronounced individual protrusions are absent, in line with fully-fused polycyclic systems. Actually, for most molecules in Figure 3a, five submolecular features, representing the five planar phenyl constituents, can be resolved. The inset in Figure 3a sketches the structure attributed to the planarized molecules, which correspond to derivative D (see Scheme 1). Note that some variability in shape and symmetry is observed for these planarized reaction products, which we attribute to the oxygen atom that can engage in ring-closing. The monomers are
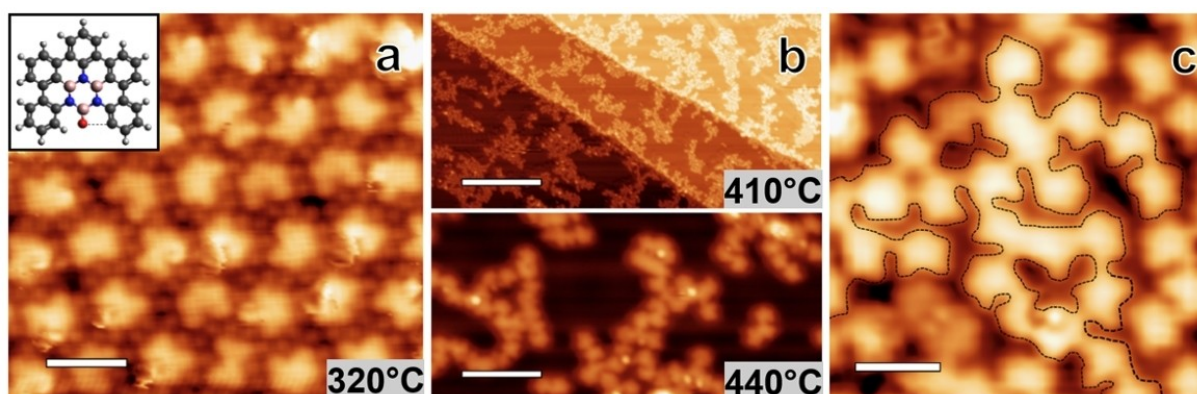

Figure 3. STM images taken after annealing at (a) 320 °C, (b lower panel) 410 °C, and (b upper panel) 440 °C respectively. Inset: Structure of a fully planarized monomer. (c) STM image of the random BNC network obtained by tetrabromoborazine deposition on Ag(111) kept at 410 °C. The superimposed black dashed lines highlight extended oligomeric segments achieved by random coupling of monomeric units. (Image parameters, (a): I_t: 99 pA, V_b: 1075 mV, scale bar: 2 nm, (b upper panel): I_t: 0.22 nA, V_b: 1078 mV, scale bar: 37 nm, (b lower panel): I_t: 68 pA, V_b: −634 mV, scale bar: 5.7 nm, (c): I_t: 0.49 nA, V_b: 284 mV, scale bar: 1.8 nm).

Chemistry–A European Journal

Research Article
doi.org/10.1002/chem.202402492

Chemistry Europe
European Chemical
Societies Publishing

surrounded by Br atoms, which might contribute to the stabilization of the observed assemblies via hydrogen bonding like C—H···Br contacts.[32,33]

Aiming at inducing intermolecular covalent coupling reactions for network formation, the molecules were annealed at 410 °C and 440 °C, respectively, as shown in the STM images in Figure 3b and c. As confirmed by XPS (see below) and consistent with literature reports,[34] Br atoms desorb from Ag(111) at these temperatures. The molecular coverage decreased in these annealing steps due to desorption. To achieve molecular coverages close to a monolayer, tetrabromoborazine was thus also directly deposited keeping the Ag substrate at a temperature of 410 °C. Both approaches (post-deposition annealing: Figure 3b, hot deposition: Figure 3c) result in percolated oligomeric structures. The STM images resolve molecular units that are connected at their peripheries (see Figure 3c), thus signalling successful intermolecular covalent C—C coupling. This final reaction product is thus assigned to a random covalent BNC-based network. The disordered character of this architecture stems from the random coupling via peripheral C—H cleavage, offering multiple sites, thus lacking selectivity. Nonetheless, as the molecular backbone including the borazine core is preserved also in this high-temperature reaction step, this stable network features a rather narrow distribution of inter-borazine distances for coupled molecular units, which range from about 0.95 to 1.35 nm. A molecular packing density of 0.59 molecule/nm² was achieved, corresponding to one borazine unit per 1.7 nm². This BN-substituted carbon network with oxygen defects is thus fundamentally different from BNC sheets synthesized by conventional CVD.

STS was employed to explore the interfacial electronic structure of the BNC network in comparison to the one of the intact precursor assembly (see Figure S2). The surface state upshift of ~220 meV exceeds that measured for the molecular assembly (~130 meV). The upshift can be governed by the adsorption distance and the molecular size.[35] If one assumes a linear dependence of the adsorption energy per surface area on the shift in surface state binding energy, as it was suggested for adsorbates physisorbed on coinage metal (111) surfaces,[36] one can estimate the adsorption energies. For the pristine tetrabromoborazine species, this yields about 14 meV/Å² (130 meV) and for the random network about 23 meV/Å² (220 meV), thus exceeding the interaction of a hBN monolayer with Ag(111) (110 meV).[37] Furthermore, the larger shift in the surface state binding energy determined for the covalent network suggests a smaller adsorption height (~0.1 Å) compared to the pristine molecular assembly,[38] which is in line with the degree of planarization.

To obtain complementary, space-averaged information on the temperature-induced on-surface reactions, XPS measurements were performed. Figure 4 shows Br 3d and O 1s core level spectra representing five distinct preparation temper-
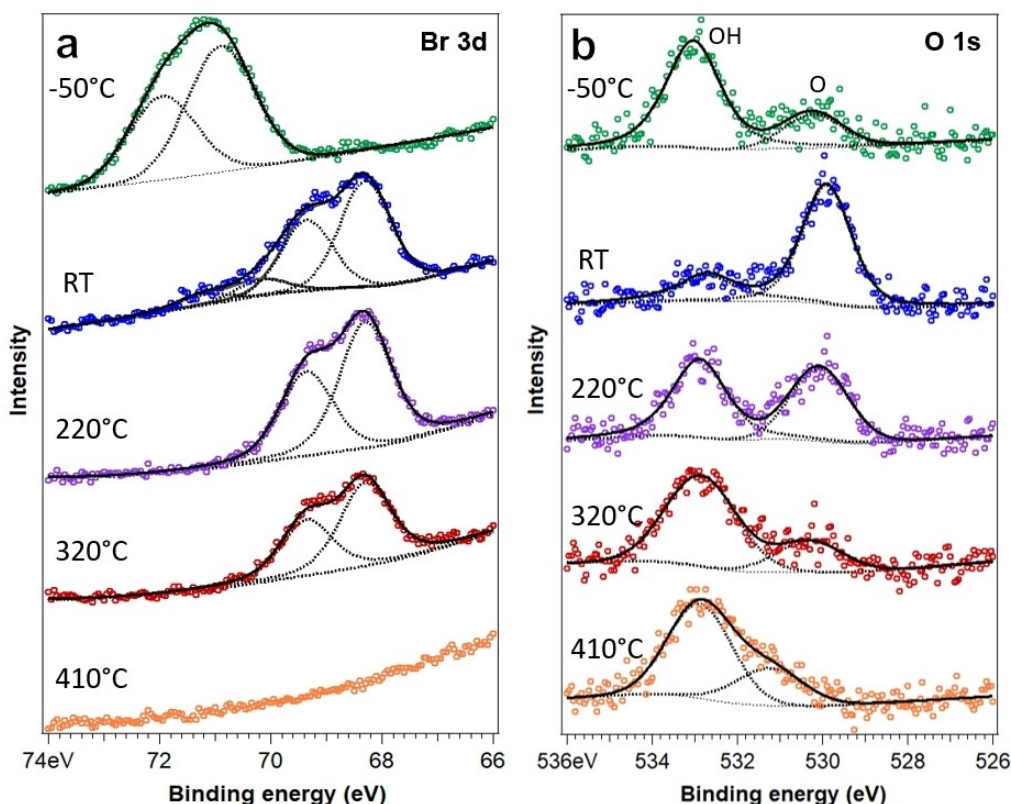

Figure 4. Evolution of (a) Br 3d doublet and (b) O 1s core level spectra with temperature. The topmost spectrum (in green) was measured at −50 °C. The other spectra were recorded at room temperature (RT, blue), after annealing to 220 °C (purple), 320 °C (red), and finally 410 °C (orange). The low binding energy component reflects carbonyl, whereas the high binding energy component is attributed to hydroxyl at low temperature and to a covalent C—O—B link at higher temperatures.

Chemistry–A European Journal

Research Article
doi.org/10.1002/chem.202402492

Chemistry
Europe
European Chemical
Societies Publishing

atures. The Br 3d data are discussed first. As mentioned above, the Br 3d spectrum obtained from tetrabromoborazine adsorbed and measured at −50 °C, reveals a doublet with the 3d3/2 component at 69.85 eV and the 3d5/2 component at 70.90 eV, corresponding to Br bonded to C,[39,40] confirming that the molecules are intact. XP spectra reflecting room temperature show contributions from two doublets. The intensity of the doublet reflecting C–Br bonds is strongly reduced compared to the low-temperature scenario. The additional doublet at lower binding energy, with the 3d5/2 component emerging at 68.2 eV is assigned to a surface component (Ag–Br), thus representing Br atoms adsorbed on Ag(111), cleaved from the phenyl rings.[39–41] The XP spectra measured after annealing at 220 °C and 320 °C only show the Ag–Br component, with reducing intensity. After annealing to 410 °C, the Br signature vanished, reflecting complete Br desorption (in line with the STM observations). We now proceed to discuss the O 1s data. At −50 °C, the O 1s signature reveals two components. The dominating higher binding energy component at 533.0 eV is attributed to hydroxyl (OH) and thus indicates that most molecules feature an intact hydroxyl group at this temperature. The lower binding energy peak at 530.2 eV is assigned to terminal oxygen (O), suggesting that a minority of the hydroxyl groups dehydrogenated. These assignments are based on the binding energies, which are in close agreement with values reported for hydroxyl and carbonyl, respectively.[42–45] It is well known that OH groups can dehydrogenate upon thermal annealing on coinage metal surfaces.[46–48] The significant increase of the lower binding energy peak, when going from low temperature to room temperature, supports our interpretation.[43,44] Interestingly, with further annealing, the relative intensity in the high binding energy region re-increases, compared to the carbonyl-like component. Clearly, a peak at 532.9 eV is observed in the spectra after annealing to 220 °C, 320 °C, and 410 °C. The recovery of OH groups is unlikely, even though hydrogen is released in the dehydrogenation steps. We rather attribute this spectral feature to oxygen engaging in an additional bond to C, forming a C–O–B link.[49] A similar re-emerging of an O 1s signal at high binding energy was reported for the temperature-induced formation of C–O–C motifs in dehydrogenated derivatives of bisphenol A and diethylstilbestrol on Cu(111).[42] The somewhat lower O 1s binding energy in our system, compared to the one reported for furan on Ag(111) (534.3 eV),[50] might be induced by the presence of B and N. Such a C–O–B moiety could emerge either from an annulation reaction[42] or from the formation of a covalent intermolecular bond. Based on the experimental findings, we propose the first scenario, i.e., a terminal oxygen links to a carbon of the adjacent phenyl moiety of the same molecule, forming an azaborole-like BOCCN ring. Such five-membered ring structures are well-characterized computationally.[51,52] It should be noted that the XPS data for 220 °C represent the hexagonal phase and the kagomé phase. The former prevails and includes a large number of molecules with fused terminal rings (see Figure S3) that can engage in bonding with the oxygen, yielding the C–O–B signature in the O 1s spectrum. Indeed, this spectral feature prevails after annealing at 320 °C, where only planarized

monomers are observed on the surface. An alternative explanation for an O 1s XPS feature with a high binding energy is atomic oxygen adsorbed on Ag(111) upon temperature-induced bond cleavage.[43] However, as STM did not provide any signature of adsorbed oxygen (and oxygen is expected to desorb from Ag(111) at the temperatures employed), we do not expect atomic oxygen to dominate the XPS fingerprint. The above discussion on the O 1s spectra has implications for the dimer structure in the kagomé phase, which will be discussed in a separate section below.

Finally, after annealing at 410 °C, the dehydrogenated component vanishes and a shoulder near the high binding energy component appears at 531.2 eV that might be related to intermolecular covalent coupling in the random BNC network. The temperature evolution of N 1s and C 1s core level spectra discussed in the Supporting Information (see Figure S5) further supports this interpretation.

Kagomé Phase and Its Electronic Structure

After the comprehensive STM and XPS characterization of tetrabromoborazine-derived reaction products achieved at different temperatures, we now revisit the intriguing kagomé phase, aiming to gain insight into the dimer's geometric and electronic structure. As discussed, dimers are formed from monomers with one or two tilted "terminal" rings (i.e., ring 1 or 5). Accordingly, it seems reasonable to assume that at least one tilted ring per molecule is a prerequisite for dimer formation. Nonetheless, a close inspection of the STM data reveals that the dimer structure, i.e., the intermolecular distance and the lateral displacement of the two constituting molecules (which induces the chiral character), is not affected by the number and position of the tilted "terminal" rings, within the experimental precision (see Figure S6). Furthermore, the dimer formation is reversible, which excludes a strong interaction. The fully planarized monomers emerging at higher temperature do not form dimers. Accordingly, one might speculate that the planarized part of the molecule, or the oxygen,[42] engage in considerable, site specific interactions with the Ag(111) support, whereas the tilted terminal ring(s) allow for a rather small intermolecular distance, thus yielding the dimer structure.

According to the interpretation of the XPS O 1s spectra (see above), most of the molecules forming the dimers present a terminal oxygen (represented by the low-binding energy feature at ~530 eV), which did not engage in the annulation reaction, as the adjacent phenyl moieties remain tilted. For molecules with one tilted terminal ring, only some arrangements seem possible, due to steric hindrance (see Figures S7 and S11). These are indeed the arrangements observed by STM, thus supporting the interpretation that intermolecular hydrogen bonding and CH···π interactions contribute to the stability of the dimers.

To further explore possible dimer configurations, DFT calculations were performed. Based on the experimental findings, dimers with a total of four (model 1), three (model 2), and two (model 3) tilted "terminal" rings were modelled (see

Chemistry–A European Journal

Research Article
doi.org/10.1002/chem.202402492

Chemistry Europe
European Chemical
Societies Publishing

Figure S7). Furthermore, intact and dehydrogenated OH groups were considered, to provide a general characterization. In order to have accessible model systems available and due to computational limitations, the calculations did not explicitly include the metal substrate. The structural models of the distinct dimer configurations are presented in the Supporting Information (Figures S8–S11), jointly with the corresponding molecular orbitals (Figures S12–S13). The supramolecular dimers of models 1–3, optimized with a fixed distance between the monomers, show very similar arrangements, regardless of the total number of tilted terminal rings (four, three, or two, Figure S11), in line with the experimental findings. Furthermore, these structures match the experimental STM data. Due to the subtle structural differences and a limited experimental precision, several of the theoretically modelled dimer structures (including intact OH groups, dehydrogenated OH groups, and covalent C–O–B links) can be reconciled with the STM data. However, only dehydrogenated supramolecular dimers (Figure S11d–f) seem consistent with the XPS data and the disappearance of dimer structures upon annealing to 320 °C.

We now turn to the interfacial electronic structure of the kagomé phase, using experimental STS point spectra and dI/dV mapping. Specifically, the electronic properties of dimers and monomers are compared. As shown in Figure 5a, point spectra measured on monomers (red curves) feature one broad resonance in the unoccupied spectral region (positive sample bias), whereas dimers reveal a double-resonance with maxima at 650 mV and 1050 mV (green and blue curves), respectively. For occupied states (negative sample bias), no features are observed in the probed bias voltage range. The double-resonance structure is observed for all dimer configurations and thus does not depend on the molecular conformation and chemical structure (i.e., the number of tilted terminal phenyl rings). This is exemplified by the spectra colored in blue and green, recorded on dimers with a total of three or four tilted rings, respectively. In order to gain more insight into the nature of this peculiar double resonance, the spatial distribution of these characteristic electronic was studied by dI/dV mapping. The acquired dI/dV maps at 650 mV and 1100 mV (see Figure 5b) reveal results consistent with the point spectroscopy: At 650 mV only dimers show high intensity, the monomer is not visible, while at 1100 mV, both the dimers and the monomers contribute. Besides minor intensity differences within dimers for both bias voltages, the spatial distribution of the electronic states differs for the two voltages. In the high energy dI/dV map, the intensity maxima are separated further than in the low energy map. The characteristics of the dI/dV maps are in line with bias-dependent STM topographic images presented in Figure S14. At 650 mV, dimers feature a larger apparent height than monomers. At 1100 mV they show similar contrast, with larger apparent spatial separation between the molecules constituting the dimers.

We assign the single peak observed for the monomers to the LUMO orbital, as it is the first feature appearing when addressing the unoccupied states. Consequently, the double-resonance structure of the dimer is described as LUMO and LUMO+1. Indeed, gas phase DFT calculations of selected dimers show a strong contribution of the LUMO and LUMO+1 orbitals on the planarized part of the molecules, in agreement with the experimental dI/dV maps (see Figures S12 and S13). The apparent splitting of the LUMO (for the monomer) into LUMO and LUMO+1 (for the dimer) is reminiscent of the
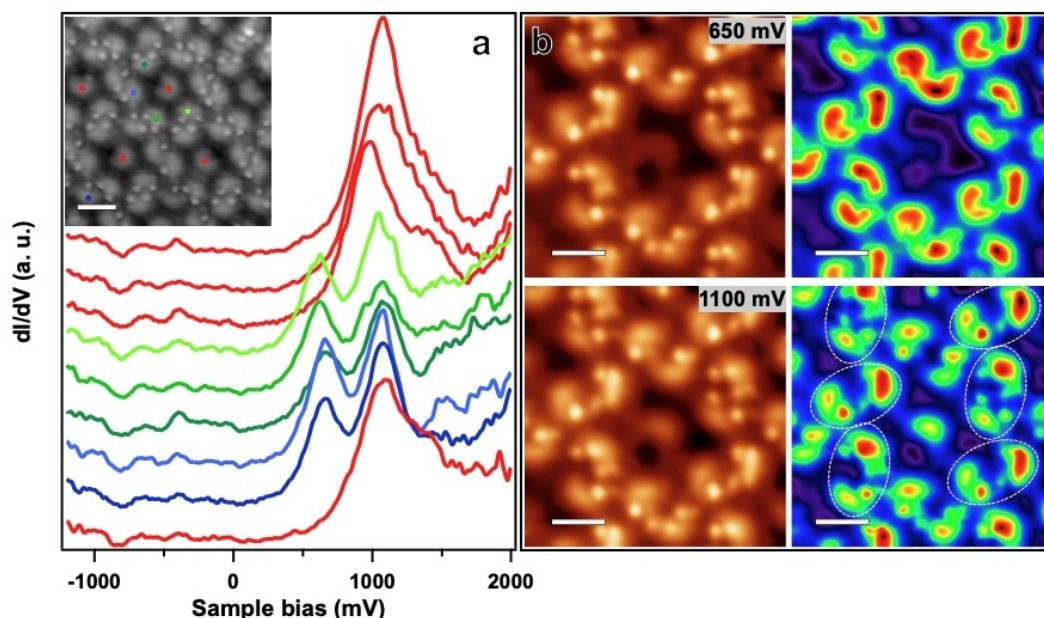

Figure 5. (a) dI/dV spectra measured on the centres of distinct molecules in the kagomé phase. Monomers are shown in red, dimer molecules featuring two tilted phenyl rings in different shades of green, and dimer molecules featuring one tilted phenyl ring in blue, respectively. The corresponding topography image is shown in the inset (scale bar: 2 nm). (V_b: 2 V, I_t: 0.13 nA, lock-in modulation voltage: 100 mV) (b) STM images (left) and the corresponding dI/dV maps measured at constant current (right). The intensity is coloured from red (high) to purple (low). (I_t: 0.13 nA, lock-in modulation voltage: 50 mV, scale bar: 1.4 nm)

Chemistry–A European Journal

Research Article
doi.org/10.1002/chem.202402492

Chemistry
Europe
European Chemical
Societies Publishing

formation of a bonding and anti-bonding orbital due to intermolecular interactions. Such a phenomenon has been experimentally reported for dimers of adatoms (Au,[53] Pb,[54]), clusters (Ca[55]) as well as molecules such as C_{60}.[56] It was also reported for molecular films, e.g., formed by stacked Sn-phthalocyanine.[57] The considerable splitting observed in our experiment (~400 mV) indicates sizeable electronic intermolecular interactions, which is surprising in view of the supramolecular dimer structure. A surface-assisted coupling mechanism, recently demonstrated to lift the LUMO degeneracy of Mg-phthalocyanine on a Ag support by intermolecular hybridization over extended distances[58] might thus contribute to the observed double-resonance structure.

Conclusions

In summary, this study provides insights into the surface chemistry of a novel functionalized borazine and gives access to intriguing BN-doped nanostructures. We demonstrate how thermally-induced chemical and structural modifications of a tetrabromoborazine precursor affect the self-assembly of the resulting derivatives. The combined XPS and STM results reveal that debromination does not promote ring-closing and planarization. Only at temperatures considerably exceeding the debromination temperature, cyclodehydrogenation occurs. This finding might contribute to an improved design of future precursors for heteroatom embedded polycyclic aromatic hydrocarbons and regular 2D-BNC materials. In case of partial molecular planarization, two coexisting architectures occur, based on distinct molecular conformations. A kagomé phase is constituted by dimers of molecules featuring tilted terminal groups adjacent to the O position, whose chirality is inherited by the assembly, whereas the hexagonal phase includes molecules with non-preferential tilting in their phenyl groups. The molecules forming the dimers have an electronic signature that differs significantly from that of the monomers. The occurrence of a split LUMO resonance, reminiscent of a bonding – antibonding pair, signals considerable electronic intermolecular interactions. We speculate that intermolecular hydrogen bonds and CH⋯π interactions contribute to the dimer formation. Selected DFT-optimized supramolecular dimer structures are consistent with the STM and XPS findings. Finally, annealing at temperatures above 400 °C, random covalent BN-doped carbon networks with oxygen defects are formed. This synthesis approach via peripheral dehydrogenative coupling of planarized molecules differs fundamentally from the established chemical vapor deposition route to BNC sheets. The resulting percolated 2D material provides a high surface density of borazine cores (~0.59/nm²). Its electronic (transport) properties remain to be explored and compared, e.g., to amorphous carbon monolayers or other BNC sheets.

Materials and Methods

Experimental

The experiments were performed in two different UHV chambers, one equipped with a CreaTec low-temperature STM (www.createc.de, base pressure of $\sim 1 \times 10^{-10}$ mbar) and one equipped with a SPECS X-ray source (Mg anode 1253.64 eV) and a SPECS PHOIBOS 100 electron analyser for XPS (base pressure of $\sim 1 \times 10^{-9}$ mbar). In both systems, the Ag(111) single-crystal was cleaned by repeated cycles of sputtering (Ar⁺ ions at an energy of 1 keV), followed by annealing at 490 °C. Tetrabromoborazine was sublimed from a quartz crucible held at ~170 °C by using a Dodecon OMBE source (www.dodecon.de), after extended degassing at 170 °C. Aiming for equal coverage, the samples were prepared by using the same deposition parameters in both chambers. STM images were acquired in constant current mode with the bias applied to the sample and processed using the WSxM software.[59] dI/dV spectroscopy was performed with open feedback loop using an internal lock-in amplifier, the parameters are indicated at the figure captions. For peak fitting, the XPST macro for IGOR (M. Schmid, Philipps University Marburg) was used. Voigt line shapes with Shirley-type or linear-parabolic backgrounds were applied, depending on the peak positions. For Br 3d, the doublet intensity ratio and doublet separation were kept fixed.

Conflict of Interests

The authors declare no conflict of interest.

Data Availability Statement

The data that support the findings of this study are available from the corresponding author upon reasonable request.

[1] L. Caputo, V. H. Nguyen, J. C. Charlier, *Phys. Rev. Mater.* **2022**, *6*, 1–9.

[2] Y. Fu, H. Yang, Y. Gao, L. Huang, R. Berger, J. Liu, H. Lu, Z. Cheng, S. Du, H. J. Gao, X. Feng, *Angew. Chem. Int. Ed.* **2020**, *59*, 8873–8879.

[3] N. Herrera-Reinoza, A. C. dos Santos, L. H. de Lima, R. Landers, A. de Siervo, *Chem. Mater.* **2021**, *33*, 2871–2882.

[4] Y. Gong, G. Shi, Z. Zhang, W. Zhou, J. Jung, W. Gao, L. Ma, Y. Yang, S. Yang, G. You, R. Vajtai, Q. Xu, A. H. Macdonald, B. I. Yakobson, J. Lou, Z. Liu, P. M. Ajayan, *Nat. Commun.* **2014**, *5*, 3193.

[5] L. Ci, L. Song, C. Jin, D. Jariwala, D. Wu, Y. Li, A. Srivastava, Z. F. Wang, K. Storr, L. Balicas, F. Liu, P. M. Ajayan, *Nat. Mater.* **2010**, *9*, 430–435.

[6] S. Beniwal, J. Hooper, D. P. Miller, P. S. Costa, G. Chen, S. Y. Liu, P. A. Dowben, E. C. H. Sykes, E. Zurek, A. Enders, *ACS Nano* **2017**, *11*, 2486–2493.

[7] L. Camilli, J. H. Jørgensen, J. Tersoff, A. C. Stoot, R. Balog, A. Cassidy, J. T. Sadowski, P. Bøggild, L. Hornekær, *Nat. Commun.* **2017**, *8*, 1–8.

[8] K. A. Bokai, A. V. Tarasov, V. O. Shevelev, O. Y. Vilkov, A. A. Makarova, D. Marchenko, A. E. Petukhov, M. Muntwiler, A. V. Fedorov, V. Y. Voroshnin, L. V. Yashina, C. Laubschat, D. V. Vyalikh, D. Y. Usachov, *Chem. Mater.* **2020**, *32*, 1172–1181.

[9] Y. Gao, Y. Zhang, P. Chen, Y. Li, M. Liu, T. Gao, D. Ma, Y. Chen, Z. Cheng, X. Qiu, W. Duan, Z. Liu, *Nano Lett.* **2013**, *13*, 3439–3443.

[10] M. G. Cuxart, D. Perilli, S. Tömekce, J. Deyerling, F. Haag, M. Muntwiler, F. Allegretti, C. Di Valentin, W. Auwärter, *Carbon* **2023**, *201*, 881–890.

[11] D. Marchionni, S. Basak, A. N. Khodadadi, A. Marrocchi, L. Vaccaro, *Adv. Funct. Mater.* **2023**, *33*, 2303635.

[12] J. Dosso, T. Battisti, B. D. Ward, N. Demitri, C. E. Hughes, P. A. Williams, K. D. M. Harris, D. Bonifazi, *Chem. Eur. J.* **2020**, *26*, 6608–6621.

[13] J. Dosso, J. Tasseroul, F. Fasano, D. Marinelli, N. Biot, A. Fermi, D. Bonifazi, *Angew. Chem. Int. Ed.* **2017**, *56*, 4483–4487.

[14] M. Krieg, F. Reicherter, P. Haiss, M. Ströbele, K. Eichele, J. Treanor, R. Schaub, H. F. Bettinger, *Angew. Chem. Int. Ed.* **2015**, *54*, 8284–8286.

[15] Z. Chen, A. Narita, K. Müllen, *Adv. Mater.* **2020**, *32*, 1–26.

[16] C. Moreno, M. Vilas-Varela, B. Kretz, A. Garcia-Lekue, M. V. Costache, M. Paradinas, A. Panighel, G. Ceballos, S. O. Valenzuela, D. Peña, A. Mugarza, *Science* **2018**, *360*, 199–203.

[17] I. Piquero-Zulaica, E. Corral-Rascón, X. Diaz de Cerio, A. Riss, B. Yang, A. Garcia-Lekue, M. A. Kher-Elden, Z. M. Abd El-Fattah, S. Nobusue, T. Kojima, K. Seufert, H. Sakaguchi, W. Auwärter, J. V. Barth, *Nat. Commun.* **2024**, *15*, 1062.

[18] S. Song, J. Su, M. Telychko, J. Li, G. Li, Y. Li, C. Su, J. Wu, J. Lu, *Chem. Soc. Rev.* **2021**, *50*, 3238–3262.

[19] C. Sánchez-Sánchez, S. Brüller, H. Sachdev, K. Müllen, M. Krieg, H. F. Bettinger, A. Nicolaï, V. Meunier, L. Talirz, R. Fasel, P. Ruffieux, *ACS Nano* **2015**, *9*, 9228–9235.

[20] S. Kawai, S. Nakatsuka, T. Hatakeyama, R. Pawlak, T. Meier, J. Tracey, E. Meyer, A. S. Foster, *Sci. Adv.* **2018**, *4*, 1–8.

[21] R. Pawlak, X. Liu, S. Ninova, P. D'Astolfo, C. Drechsel, J. C. Liu, R. Häner, S. Decurtins, U. Aschauer, S. X. Liu, E. Meyer, *Angew. Chem. Int. Ed.* **2021**, *60*, 8370–8375.

[22] R. Pawlak, X. Liu, S. Ninova, P. D'Astolfo, C. Drechsel, S. Sangtarash, R. Häner, S. Decurtins, H. Sadeghi, C. J. Lambert, U. Aschauer, S. X. Liu, E. Meyer, *J. Am. Chem. Soc.* **2020**, *142*, 12568–12573.

[23] K. Sun, O. J. Silveira, S. Saito, K. Sagisaka, S. Yamaguchi, A. S. Foster, S. Kawai, *ACS Nano* **2022**, *16*, 11244–11250.

[24] N. Kalashnyk, P. Ganesh Nagaswaran, S. Kervyn, M. Riello, B. Moreton, T. S. Jones, A. De Vita, D. Bonifazi, G. Costantini, *Chem. – A Eur. J.* **2014**, *20*, 11856–11862.

[25] M. Schwarz, M. Garnica, F. Fasano, N. Demitri, D. Bonifazi, W. Auwärter, *Chem. – A Eur. J.* **2018**, *24*, 9565–9571.

[26] A. Belser, K. Greulich, P. Grüninger, H. F. Bettinger, H. Peisert, T. Chassé, *ACS Appl. Mater. Interfaces* **2020**, *12*, 19218–19225.

[27] T. Weiss, A. Baklanov, G. S. Michelitsch, K. Reuter, M. Schwarz, M. Garnica, W. Auwärter, *Adv. Mater. Interfaces* **2024**, *11*, 1–10.

[28] S. Kervyn, N. Kalashnyk, M. Riello, B. Moreton, J. Tasseroul, J. Wouters, T. S. Jones, A. De Vita, G. Costantini, D. Bonifazi, *Angew. Chem. Int. Ed.* **2013**, *52*, 7410–7414.

[29] Y. Makoudi, M. Beyer, J. Jeannoutot, F. Picaud, F. Palmino, F. Chérioux, *Chem. Commun.* **2014**, *50*, 5714–5716.

[30] K. A. Simonov, A. V. Generalov, A. S. Vinogradov, G. I. Svirskiy, A. A. Cafolla, C. McGuinness, T. Taketsugu, A. Lyalin, N. Mårtensson, A. B. Preobrajenski, *Sci. Rep.* **2018**, *8*, 3506.

[31] L. Talirz, H. Söde, J. Cai, P. Ruffieux, S. Blankenburg, R. Jafaar, R. Berger, X. Feng, K. Müllen, D. Passerone, R. Fasel, C. A. Pignedoli, *J. Am. Chem. Soc.* **2013**, *135*, 2060–2063.

[32] J. Lu, Z. Ruan, Y. Guan, D.-L. Bao, X. Lin, Z. Hao, H. Zhang, L. Song, C. Yan, J. Cai, S. Du, H.-J. Gao, *J. Phys. Chem. C* **2018**, *122*, 25681–25684.

[33] J. Lu, D. L. Bao, H. Dong, K. Qian, S. Zhang, J. Liu, Y. Zhang, X. Lin, S. X. Du, W. Hu, H. J. Gao, *J. Phys. Chem. Lett.* **2017**, *8*, 326–331.

[34] M. Fritton, D. A. Duncan, P. S. Deimel, A. Rastgoo-Lahrood, F. Allegretti, J. V. Barth, W. M. Heckl, J. Björk, M. Lackinger, *J. Am. Chem. Soc.* **2019**, *141*, 4824–4832.

[35] N. L. Zaitsev, I. A. Nechaev, P. M. Echenique, E. V. Chulkov, *Phys. Rev. B – Condens. Matter Mater. Phys.* **2012**, *85*, 1–8.

[36] J. Ziroff, P. Gold, A. Bendounan, F. Forster, F. Reinert, *Surf. Sci.* **2009**, *603*, 354–358.

[37] M. Garnica, M. Schwarz, J. Ducke, Y. He, F. Bischoff, J. V. Barth, W. Auwärter, D. Stradi, *Phys. Rev. B* **2016**, *94*, 1–6.

[38] N. Armbrust, F. Schiller, J. Güdde, U. Höfer, *Sci. Rep.* **2017**, *7*, 46561.

[39] R. Gutzler, L. Cardenas, J. Lipton-Duffin, M. El Garah, L. E. Dinca, C. E. Szakacs, C. Fu, M. Gallagher, M. Vondráček, M. Rybachuk, D. F. Perepichka, F. Rosei, *Nanoscale* **2014**, *6*, 2660–2668.

[40] L. Cardenas, R. Gutzler, J. Lipton-Duffin, C. Fu, J. L. Brusso, L. E. Dinca, M. Vondráček, Y. Fagot-Revurat, D. Malterre, F. Rosei, D. F. Perepichka, *Chem. Sci.* **2013**, *4*, 3263–3268.

[41] J. Eichhorn, T. Strunskus, A. Rastgoo-Lahrood, D. Samanta, M. Schmittel, M. Lackinger, *Chem. Commun.* **2014**, *50*, 7680–7682.

[42] P. S. Deimel, K. Stoiber, L. Jiang, J. A. Lloyd, S. C. Oh, S. Fischer, Ö. Saglam, H. Schlichting, A. C. Papageorgiou, J. V. Barth, F. Allegretti, J. Reichert, *J. Phys. Chem. C* **2019**, *123*, 1354–1361.

[43] B. Yang, N. Cao, H. Ju, H. Lin, Y. Li, H. Ding, J. Ding, J. Zhang, C. Peng, H. Zhang, J. Zhu, Q. Li, L. Chi, *J. Am. Chem. Soc.* **2019**, *141*, 168–174.

[44] L. Feng, T. Wang, Z. Tao, J. Huang, G. Li, Q. Xu, S. L. Tait, J. Zhu, *ACS Nano* **2019**, *13*, 10603–10611.

[45] Q. Li, B. Yang, H. Lin, N. Aghdassi, K. Miao, J. Zhang, H. Zhang, Y. Li, S. Duhm, J. Fan, L. Chi, *J. Am. Chem. Soc.* **2016**, *138*, 2809–2814.

[46] F. Bebensee, K. Svane, C. Bombis, F. Masini, S. Klyatskaya, F. Besenbacher, M. Ruben, B. Hammer, T. Linderoth, *Chem. Commun.* **2013**, *49*, 9308–9310.

[47] A. G. Slater, L. M. A. Perdigão, P. H. Beton, N. R. Champness, *Acc. Chem. Res.* **2014**, *47*, 3417–3427.

[48] R. Pawlak, S. Clair, V. Oison, M. Abel, O. Ourdjini, N. A. A. Zwaneveld, D. Gigmes, D. Bertin, L. Nony, L. Porte, *ChemPhysChem* **2009**, *10*, 1032–1035.

[49] B. J. Matsoso, K. Ranganathan, B. K. Mutuma, T. Lerotholi, G. Jones, N. J. Coville, *New J. Chem.* **2017**, *41*, 9497–9504.

[50] T. Paintner, J. Björk, P. Du, S. Klyatskaya, M. Paszkiewicz, R. Hellwig, M. Uphoff, M. A. Öner, E. Cuniberto, P. S. Deimel, Y. Q. Zhang, C. A. Palma, F. Allegretti, M. Ruben, J. V. Barth, F. Klappenberger, *Angew. Chem. Int. Ed.* **2019**, *58*, 11285–11290.

[51] V. A. Dixit, W. R. F. Goundry, S. Tomasi, *New J. Chem.* **2017**, *41*, 3619–3633.

[52] R. J. Doerksen, *J. Phys. Chem. A* **1999**, *103*, 2141–2151.

[53] N. Nilius, T. M. Wallis, M. Persson, W. Ho, *Phys. Rev. Lett.* **2003**, *90*, 4.

[54] J. W. Park, H. S. Kim, T. Brumme, T. Heine, H. W. Yeom, *Nat. Commun.* **2020**, *11*, 1–6.

[55] W. Ko, C. Ma, G. D. Nguyen, M. Kolmer, A. P. Li, *Adv. Funct. Mater.* **2019**, *29*, 1–24.

[56] M. Feng, J. Zhao, H. Petek, *Science* **2008**, *320*, 359–363.

[57] Y. Kashimoto, K. Yonezawa, M. Meissner, M. Gruenewald, T. Ueba, S. Kera, R. Forker, T. Fritz, H. Yoshida, *J. Phys. Chem. C* **2018**, *122*, 12090–12097.

[58] M. Castelli, J. Hellerstedt, C. Krull, S. Gicev, L. C. L. Hollenberg, M. Usman, A. Schiffrin, *Small* **2021**, *17*, 1–10.

[59] I. Horcas, R. Fernández, J. M. Gómez-Rodríguez, J. Colchero, J. Gómez-Herrero, A. M. Baro, *Rev. Sci. Instrum.* **2007**, *78*, 013705.